CCFE
CULHAM CENTRE FOR FUSION ENERGY

UK Atomic Energy Authority

UKAEA-CCFE-PR(23)116

Mark Fedorov, Jan S. Wróbel, Andrew J. London, Krzysztof J. Kurzydłowski, Chu-Chun Fu, Tonči Tadić, Sergei L. Dudarev, Duc Nguyen-Manh

Radiation-induced precipitation of chromium in Fe-Cr alloys containing C and N impurities: First-principles modelling and experimental observations

Radiation-induced precipitation of chromium in Fe-Cr alloys containing C and N impurities: First-principles modelling and experimental observations

Mark Fedorov, Jan S. Wróbel, Andrew J. London, Krzysztof J. Kurzydłowski, Chu-Chun Fu, Tonči Tadić, Sergei L. Dudarev, Duc Nguyen-Manh

This is a preprint of a paper submitted for publication in Acta Materialia

Graphical Abstract

Radiation-induced precipitation of chromium in Fe-Cr alloys containing C and N impurities: First-principles modelling and experimental observations

Mark Fedorov,Jan S. Wróbel,Andrew J. London,Krzysztof J. Kurzydłowski,Chu-Chun Fu,Tonči Tadić,Sergei L. Dudarev,Duc Nguyen-Manh

Highlights

Radiation-induced precipitation of chromium in Fe-Cr alloys containing C and N impurities: First-principles modelling and experimental observations

Mark Fedorov,Jan S. Wróbel,Andrew J. London,Krzysztof J. Kurzydłowski,Chu-Chun Fu,Tonči Tadić,Sergei L. Dudarev,Duc Nguyen-Manh

- Anomalous precipitation of Cr in Fe-rich Fe-Cr alloys is predicted by *ab initio* modelling, the effect is confirmed by experimental observations
- Increased local Cr concentration is correlated with the local interstitial impurity content
- The driving force for Cr precipitation is the high stability of $[Fe_xCr_y]_3[C_aN_b]$ ordered compounds

Radiation-induced precipitation of chromium in Fe-Cr alloys containing C and N impurities: First-principles modelling and experimental observations

Mark Fedorov[a], Jan S. Wróbel[a], Andrew J. London[b,c], Krzysztof J. Kurzydłowski[d], Chu-Chun Fu[e], Tonči Tadić[f], Sergei L. Dudarev[b,c] and Duc Nguyen-Manh[b,c]

[a]Faculty of Materials Science and Engineering, Warsaw University of Technology, ul. Wołoska 141, 02-507 Warsaw, Poland
[b]CCFE, UK Atomic Energy Authority, Culham Science Centre, Abingdon, OX14 3DB, United Kingdom
[c]Department of Materials, University of Oxford, Oxford, OX1 3PH, United Kingdom
[d]Faculty of Mechanical Engineering, Białystok University of Technology, Poland
[e]Université Paris-Saclay, CEA, Service de Recherches de Métallurgie Physique, F-91191 Gif-sur-Yvette, France
[f]Division of Experimental Physics, Ruđer Bošković Institute, Zagreb, Croatia

ARTICLE INFO

Keywords:
Irradiation effects
Fe Cr alloys
anomalous Cr precipitation
Density Functional Theory (DFT)
Cluster expansion
Monte Carlo simulations
Atom Probe Tomography (APT)
carbon and nitrogen impurities

ABSTRACT

Using exchange Monte Carlo (MC) simulations based on an *ab initio*-parameterized Cluster Expansion (CE) model, we explore the phase stability of low-Cr Fe-Cr alloys as a function of vacancy (Vac), carbon, and nitrogen interstitial impurity content. To parameterise the CE model, we perform density functional theory calculations for more than 1600 supercells containing Cr-Vac-C-N clusters of various size in pure bcc Fe, Cr, and Fe-Cr alloys. Our analysis shows that including three-body cluster interactions in a CE model is necessary for achieving agreement with experimental observations. MC simulations performed for $T = 650$K show that Cr clustering in Fe-3.28%Cr alloys does not occur if there are no defects or if only vacancies are present. But the addition of a small amount of C or N impurities, at the level as low as 0.02 at.% in an alloy with no vacancies, routinely results in the formation of ordered interstitial compounds containing a high amount of Cr. We find that Cr segregates to interstitial impurities and that the local Cr content increases as a function of C and/or N concentration in a Fe-Cr alloy. In the presence of vacancies, C/N impurities aggregate to the core regions of vacancy clusters (voids), making Cr segregation effects less pronounced. The structure of Cr-rich clusters varies significantly, depending on the impurity content and on the N to C ratio. Predictions derived from MC simulations agree with experimental observations of Fe-Cr alloys exposed to ion irradiation. The concentration of Cr found in clusters with C and N interstitial impurities is in qualitative agreement, and the absolute Cr content found in the clusters simulated at 650 K is in quantitative agreement with experimental atom probe tomography (APT) observations of Fe-3.28%Cr alloys irradiated at 623 K, where the measured C and N content of 42±5 and 151±3 atomic ppm likely resulted from the contamination occurred during ion beam irradiation.

1. Introduction

Ferritic-martensitic Fe-Cr-based alloys and steels, including EUROFER and ferritic ODS steels, are among the materials selected for DEMO first wall and structural applications [1]. EUROFER steel offers a good overall balance between mechanical properties, corrosion resistance and good stability under irradiation, exhibiting relatively low swelling [2, 3]. However, these steels exhibit radiation hardening at low temperature even at a moderate radiation exposure. A possible reason for the loss of mechanical properties is the formation of precipitates of Cr-rich α'-phase [4, 5, 6, 7] observed even in irradiated alloys with Cr concentration below the Cr solubility limit [8]. This effect appears to be associated with the radiation-driven clustering of chromium atoms, resulting in the formation of Cr-rich precipitates. The authors of Refs. [4, 7, 9] proposed that Cr precipitates were associated with dislocation loops. This suggestion was seemingly supported by studies of crystallographic orientations of Cr clusters that appeared consistent with the habit planes of dislocation loops in bcc Fe-based alloys [7]. On the other hand, Haley *et al.* [5] observed that Cr-rich clusters in irradiated Fe-9%Cr alloys were consistently characterised by spherical or faceted geometry. This suggests that there might be another driving force, different from elastic fields of dislocation loops, responsible for the formation of Cr-rich clusters forming in the irradiated relatively dilute Fe-Cr alloys. According to the investigation of HCM12A and T91 alloys by Jiao *et al.* [9], there are competing sinks for Cr, including grain boundaries, phase interfaces, dislocations and inhomogeneously distributed ordered Cr phases. For the latter ones, the mechanism of formation may involve point defects.

Hypothetically, vacancies or interstitial impurities like carbon (C), nitrogen (N), or oxygen (O), might be responsible for Cr clustering. The very high concentration of vacan-

*Corresponding author: Jan.Wrobel@pw.edu.pl
**Corresponding author: Duc.Nguyen@ukaea.uk
mark.fedorov.dokt@pw.edu.pl (M. Fedorov); jan.wrobel@pw.edu.pl (J.S. Wróbel); andy.london@ukaea.uk (A.J. London); k.kurzydlowski@pb.edu.pl (K.J. Kurzydłowski); chuchun.fu@cea.fr (C. Fu); tonci.tadic@irb.hr (T. Tadić); sergei.dudarev@ukaea.uk (S.L. Dudarev); duc.nguyen@ukaea.uk (D. Nguyen-Manh)
ORCID(s): 0000-0001-9211-2664 (M. Fedorov); 0000-0002-3542-5127 (J.S. Wróbel); 0000-0001-6959-9849 (A.J. London); 0000-0003-3875-4820 (K.J. Kurzydłowski); 0000-0003-4369-8296 (C. Fu); 0000-0002-7954-3547 (S.L. Dudarev); 0000-0001-6061-9946 (D. Nguyen-Manh)

cies in irradiated alloys stems from the generation of Frenkel pairs [10]. On the other hand, C, N or O atoms are always present in steels, either as alloying elements or as impurities. Recent atom probe tomography (APT) experiments showed that impurities at concentrations as low as a few appm affect the structural evolution of alloys under irradiation. Kuksenko *et al.* [7] observed the co-segregation of Ni, Si and P in Cr-rich clusters in Fe-Cr alloys with Cr content varying in the interval from 2.5, 5, 9 to 12 at. %. Moreover, in Fe-2.5%Cr alloys, higher concentration of C was found in Cr-rich clusters. Cr carbides were observed also in proton irradiated HCM12A alloy by Swenson *et al.* [11], whereas traces of nitrogen in the regions of Cr enrichment were detected in irradiated Fe-5%Cr alloys by Hardie *et al.* [4]. Authors of Ref. [12] also described the formation of carbides and nitrides in Fe-15%Cr alloys, but in a study of Fe-(3–18)%Cr set of alloys [13] they noted that clustering of Cr under irradiation occurred only if the Cr content exceeded 6%. Finally, Haley *et al.* [5] ruled out the possibility of formation of chromium oxides in the clusters, as they observed no oxygen in the clusters.

This study focuses on the effect of C and N impurities on the phase stability and microstructure of Fe-Cr alloys, which also contain vacancies as a feature associated with the effect of irradiation.

Although the formation of Cr-rich phases in irradiated Fr-Cr alloys with low Cr content can be attributed to the interaction between radiation point defects, impurities and Cr atoms in bcc Fe matrix, the exact nature of the processes responsible for Cr precipitation remain unclear. Earlier theoretical studies performed using Density Functional Theory (DFT) showed that C, N and O impurities strongly interact with vacancies, forming highly stable vacancy-solute clusters [14, 15, 16, 17]. Vacancies give rise to the effective attraction between C or N impurities that otherwise repel each other in pure bcc Fe matrix. Vacancies also attract Cr atoms [18] and together with C they may form energetically stable Vac-Cr-C clusters [19]. However, it is not clear if these vacancy-mediated interactions can drive the segregation of Cr atoms in bcc Fe matrix.

Multi-scale models for Fe-Cr alloys and compounds, treating atomic exchange [17], atomic-level kinetic [20, 21] and object kinetic [22] Monte Carlo (MC) simulations, helped improve the understanding of structural stability of those alloys. To the best of our knowledge, none of these models explained why Cr-rich precipitates formed in irradiated Fe-Cr alloys with Cr concentration below the Cr solubility limit.

In this study, we investigate the phase stability of Fe-3.28%Cr alloys containing vacancies and C and N impurities. We use a combination of DFT, Cluster Expansion (CE) method and MC simulations, described in Section 2 of the paper, and perform experiments to validate our model, see Section 3. A similar theoretical approach was successful in explaining the anomalous segregation of Re and Os in irradiated dilute W-Re and W-Re-Os alloys [23, 24]. The new lattice model for the Fe-Cr-Vac-C-N system introduces a second sublattice, in addition to the main bcc lattice, to describe the octahedral sites. The octahedral sites can be occupied by C or N impurities. The various binding energies are analysed in Section 4, whereas in the subsequent sections we summarise the results of MC simulations (Section 5) and APT experiments (Section 6). Simulations and observations describing Fe-3.28%Cr alloys are compared in Section 7.

2. Computational methods

The constrained thermodynamic equilibrium of Fe-Cr-Vac-C-N system as a function of composition, including the vacancy content and temperature, was investigated using a combination of Density Functional Theory (DFT), Cluster Expansion (CE) and Monte Carlo (MC) simulations. Such a methodology, applied earlier to W-Re-Vac alloys, explained the origin of clustering of Re atoms in irradiated W-Re and W-Re-Os alloys with low Re and Os content, see [23, 24]. As an extension of these models, here the DFT-CE-MC methodology was applied to an alloy where atoms can occupy two different sublattices: (i) a sublattice of bcc sites, occupied by Fe or Cr atoms, or bcc vacancies, and (ii) a sublattice of octahedral sites, occupied by C or N atoms, or by the "octahedral lattice" vacancies. Vacancies on different sublattices are not interchangeable – for example, a bcc Vac is a real point defect on the bcc sublattice, whereas an octahedral Vac simply represents an unoccupied octahedral site. Fig. 1 shows a schematic view of the two sublattices, indicating the distances pertinent to the definition of the relevant binding energies.

To construct a CE model, DFT calculations were performed for the following groups of atomic structures:

1. Ordered Fe-Cr structures involving various primitive unit cells and a 2x2x2 conventional supercell, including the structures with interstitial clusters of C/N/C+N.
2. Clusters with Cr(Fe), Vac, N, C in bcc Fe(Cr) matrix in a 4x4x4 supercell. These include 2-, 3-, and 4-body clusters.
3. Compact 8-atom clusters of Cr atoms or vacancies (voids), defined using 4x4x4 and 5x5x5 supercells.
4. α-cementite-type structures – a prototype of a bcc precursor to iron carbide – including the structures based on bcc 12-atom SQS Fe-Cr matrix and their derivatives, containing vacancies and various amounts of C and N. Fig. 2 provides a visual representation of this type of structures.

The full DFT database of Fe-Cr-Vac-C-N configurations used in this study comprises 1671 atomic structures.

DFT calculations were performed assuming collinear spin polarization, using the projector augmented wave (PAW) method implemented in VASP [25, 26, 27, 28, 29, 30]. Exchange and correlation were treated in the generalized gradient GGA-PBE approximation [31]. The core configurations of Fe, Cr, C and N ions in the PAW potentials were taken as $[Ar]3d^74s^1$, $[Ar]3d^54s^1$, $[He]2s^22p^2$, $[He]2s^22p^3$, respectively.

The total DFT energies of various structures were evaluated using a Γ-centered Monkhorst-Pack mesh [32] of k-points in the Brillouin zone, with the k-mesh spacing of 0.2 Å^{-1}.

Figure 1: Visualization of distances in a bcc unit cell: bcc lattice sites are shown as squares, octahedral sites are shown as circles. Each site is characterised by its two-lattice nearest neighbour (nn) position with respect to the origin of the Cartesian coordinate system, situated at the bottom left corner of the diagram. Some of the sites (e.g. site 4) can only be occupied by atoms belonging to the bcc lattice. If the origin were chosen to reside on the octahedral lattice (e.g. on site 2 indicated by a solid circle), there would have been an asymmetry of similar kind. Examples of the first three nn, involving pairs of sites on the two sublattices, are shown in identical colors – green, blue and red for the 1nn, 2nn and 3nn sites, respectively. Labels next to the bcc sites indicate distances given in the units of the bcc nearest neighbour distance (NN).

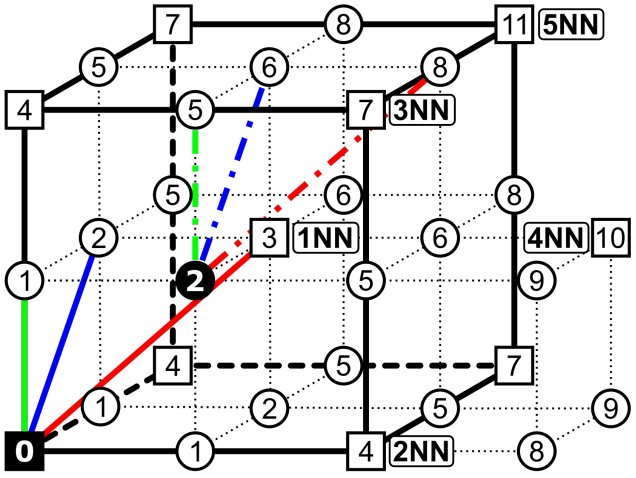

This corresponds to a 14x14x14 k-point mesh for a conventional bcc unit cell. The plane wave cutoff energy used in the calculations was 400 eV. The total energy convergence criterion was set to 10^{-6} eV/cell, and the force components relaxation cutoff was set to $5 \cdot 10^{-3}$ eV/Å.

The binding energies of defect clusters were assessed to verify if a clustered configuration were energetically favourable compared to separate defects, in various alloy configurations. The energies were computed as follows:

$$\begin{aligned} &E_{bind}(a \cdot \mathrm{C},\ b \cdot \mathrm{N},\ c \cdot \mathrm{Vac},\ d \cdot \mathrm{Cr}) = \\ &a \cdot E_{tot}(1 \cdot \mathrm{C}) + b \cdot E_{tot}(1 \cdot \mathrm{N}) + \\ &c \cdot E_{tot}(1 \cdot \mathrm{Vac}) + d \cdot E_{tot}(1 \cdot \mathrm{Cr}) - \\ &E_{tot}(a \cdot \mathrm{C},\ b \cdot \mathrm{N},\ c \cdot \mathrm{Vac},\ d \cdot \mathrm{Cr}) - \\ &\qquad (a + b + c + d - 1) \cdot E(\mathrm{Fe}) \end{aligned} \quad (1)$$

where a is the number of C atoms, b is the number of N atoms, c is the number of vacancies, d is the number of Cr atoms in the Fe matrix. $E_{tot}(1 \cdot C)$, $E_{tot}(1 \cdot N)$, $E_{tot}(1 \cdot Vac)$, $E_{tot}(1 \cdot Cr)$ and $E_{tot}(a \cdot C,\ b \cdot N,\ c \cdot Vac,\ d \cdot Cr)$ are the total energies of Fe supercells containing one C atom, one N atom, one vacancy, one Cr atom and a cluster of these atoms, respectively. A positive value of the binding energy implies that defects attract each other and can form a cluster, whereas a negative value of E_{bind} indicates that that the formation of a defect cluster is energetically not favourable

Figure 2: Sketch of α-cementite, treated as a bcc precursor of the cementite phase. Bcc sites are shown as squares, whereas occupied octahedral sites are shown as circles. A black cube in the middle of the diagram represents a conventional bcc unit cell. The red parallelepiped represents an α-cementite primitive cell. Unit vectors of the primitive lattice are given in the nn, NN and lattice parameter (a) units. The shortest distance between a pair of two occupied octahedral sites is either 5nn (cyan dash-dotted lines) or 6nn (pink dotted lines).

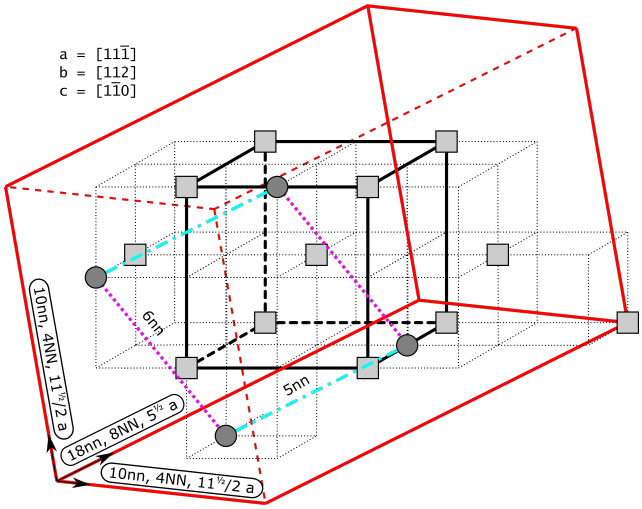

and, if created, such a cluster would decompose into separate individual point defects.

To investigate the finite-temperature phase stability, it is necessary to first evaluate the stability at 0 K, defined by the enthalpy of mixing H_{mix}, and then create a Cluster Expansion model and optimize the mapping of H_{mix} from DFT to CE to maximise the predictive capability of the model.

The enthalpy of mixing for a chosen alloy configuration, defined by a vector of configurational variables $\vec{\sigma}$ and evaluated using DFT, can be written as follows,

$$H_{mix}^{DFT}(\vec{\sigma}) = E_{tot}(\vec{\sigma}) - \sum_{p=1}^{K} c_p E_{tot}^{ref}(p), \quad (2)$$

where $E_{tot}(\vec{\sigma})$ is the total energy of the configuration, $E_{tot}^{ref}(p)$ is a reference energy corresponding to pure component p, K is the number of alloy components and c_p is the average concentration of each component.

Once the values of H_{mix}^{DFT} were computed for all the structures included in the database, the structure inversion method was applied to generate a CE parameterization. In the CE model, the enthalpy of mixing H_{mix}^{CE} is given by

$$H_{mix}^{CE} = \sum_{\omega,n,s} J_{\omega,n}^{(s)} m_{\omega,n}^{(s)} \left\langle \Gamma_{\omega,n}^{(s)}(\vec{\sigma}) \right\rangle. \quad (3)$$

Summation here is performed over all the clusters, distinct under symmetry operations in the two-sublattice model and described by the following parameters: ω is the number of lattice points ("bodies") in the cluster, n is the largest distance between two points in the cluster defined in terms of

the nearest neighbour classification of the two-sublattice model (nn), and (s) is the decoration of the cluster, i.e. the occupation of the lattice points by atoms of different kind in varying order. $J^{(s)}_{\omega,n} m^{(s)}_{\omega,n}$ is the effective cluster interaction in each cluster, $m^{(s)}_{\omega,n}$ is the site multiplicity of each cluster (in per-lattice-site units). $\left\langle \Gamma^{(s)}_{\omega,n}(\vec{\sigma}) \right\rangle$ are the so-called cluster functions, averaged over all the clusters with the same parameters.

A cluster function $\Gamma^{(s)}_{\omega,n}(\vec{\sigma})$ is a product of orthonormal point functions of occupation variables $\gamma_{j,K}(\sigma_i)$ for each cluster with the same ω and n,

$$\Gamma^{(s)}_{\omega,n}(\vec{\sigma}) = \gamma_{j_1,K}(\sigma_1)\gamma_{j_2,K}(\sigma_2)\dots\gamma_{j_\omega,K}(\sigma_\omega). \quad (4)$$

Sequence $(s) = (j_1, j_2, \dots, j_\omega)$ is the decoration of a cluster by point functions, where a point function is defined as

$$\gamma_{j,K}(\sigma_i) = \begin{cases} 1 & \text{if } j = 0\,, \\ -\cos\left(2\pi \left\lceil \frac{j}{2} \right\rceil \frac{\sigma_i}{K}\right) & \text{if } j > 0 \text{ and odd}, \\ -\sin\left(2\pi \left\lceil \frac{j}{2} \right\rceil \frac{\sigma_i}{K}\right) & \text{if } j > 0 \text{ and even}, \end{cases} \quad (5)$$

where $\sigma_i = i = 0, 1, 2, ...(K-1)$ is a number representing constituent components of a K-component alloy, j is the index of point functions $j = 0, 1, 2, ...(K-1)$, and $\left\lceil \frac{j}{2} \right\rceil$ is the ceiling function that rounds up a rational number to the closest integer.

The mapping of H_{mix}, derived from DFT calculations, to H_{mix} obtained from a CE model, parameterised using the structures included in the database, was done using the ATAT package [33, 34, 35, 36]. The CE method has been recently extended to include voids decorated by transmutation products in tungsten irradiated at high temperatures [23, 24].

The predictive accuracy of a CE model can be quantitatively evaluated using the cross-validation score (CVS) [33]

$$CVS^2 = \frac{1}{N}\sum_{i=1}^{N}\left(E^i_{DFT} - E^{(i)}_{CE'}\right)^2, \quad (6)$$

where $E^{(i)}_{CE'}$ is the energy of the i-th structure, predicted by fitting the CE energies to DFT energies, excluding E^i_{DFT} of the i-th structure.

Various sets of Effective Cluster Interactions (ECIs) were tested to find the best (minimum) CVS between the DFT and CE energies. The final set of ECIs includes pairwise interactions up to the third nearest-neighbour coordination shell in bcc lattice and 3-body interactions involving up to the second nearest-neighbour coordination shell in bcc lattice.

Semi-canonical exchange MC simulations were performed using `memc2` subroutine of the ATAT package. Various supercell sizes have been tested, going up to 49x49x49 bcc unit cells, and a 37x37x37 supercell was selected as the optimal choice from the perspective of representability of the observed structures and the time cost. The optimal number of equilibration and accumulation Monte Carlo steps is 2000 per atom – this value has been used in all the MC simulations. For each composition, simulations were performed assuming a fixed temperature of 650 K, and starting from a disordered state.

2.1. DFT and CE model overview

Comparison of mixing enthalpies deduced from DFT and CE for the entire Fe-Cr-Vac-C-N database is given in Fig. 3(a), where Fe-Cr structures without vacancies and interstitials are shown separately. Notably, the model is able to reproduce the region of Fe-rich structures characterised by negative values of H_{mix}. By comparing the enthalpies of mixing of non-defective Fe-Cr structures and those containing defects, we conclude that the addition of the latter can drastically change H_{mix} and stabilize or destabilize the corresponding structures. Among the ordered structures, the lowest enthalpies of formation correspond to structures based on the α-cementite Fe_3C phase (which is a potential bcc precursor of the cementite phase [37]) where some of the Fe and C atoms are replaced by Cr and N, respectively (see Fig. 3(b)).

The enthalpies of formation of α-cementite-like structures $[Fe_xCr_y]_3[C_aN_b]$, where x, y denote the concentration of the corresponding alloy components on the bcc sublattice, and a, b on the octahedral sublattice, are shown in Fig. 3(b). The most stable structures across the entire concentration range are the ones containing only nitrogen (N) on the interstitial sublattice. All these structures have negative formation enthalpies. The least stable are the structures containing only C on the interstitial sublattice, and all of them have positive formation enthalpies. The most stable mixed structures at each Cr concentration are those involving both N and C interstitial impurities, and characterised by a C to N ratio as a significant physical parameter. We also note that the enthalpies of formation of $[Fe_xCr_y]_3[C_aN_b]$ phases decrease as a function of Cr content. In the next section we discuss how this phenomenon might be responsible for the formation of Cr-rich clusters in Fe-Cr alloys containing Cr concentration below the solubility limit.

The values of effective cluster interaction parameters are given in the Supplementary Material [38]. The cross-validation score for the final mapping of H^{DFT}_{mix} to H^{CE}_{mix} is 5 meV, which corresponds to the error margin of ∼60 K in the Monte Carlo simulations described below.

3. Materials and Experimental Methods

3.1. Materials and preparation

Ultra high purity polycrystalline Fe 3wt%Cr and Fe 5wt%Cr alloys were produced by EFDA under contract EFDA-06-1901 [39]. Chemical analysis of the alloys in the as-received condition showed for one of the alloys 5.40 wt% Cr and in atomic ppm: C 4, S 3, O 6, N 2 and less than 5 P. The Fe3wt%Cr alloy contained 3.05wt% Cr and in atomic ppm: C 4, S 3, O 4, N 2 and <5 P. The specimens were cut (25x1x1 mm) by electrode discharge machining and surface damage removed using SiC abrasive paper of various grades, before polishing with 9 um and 1 um diamond paste followed by

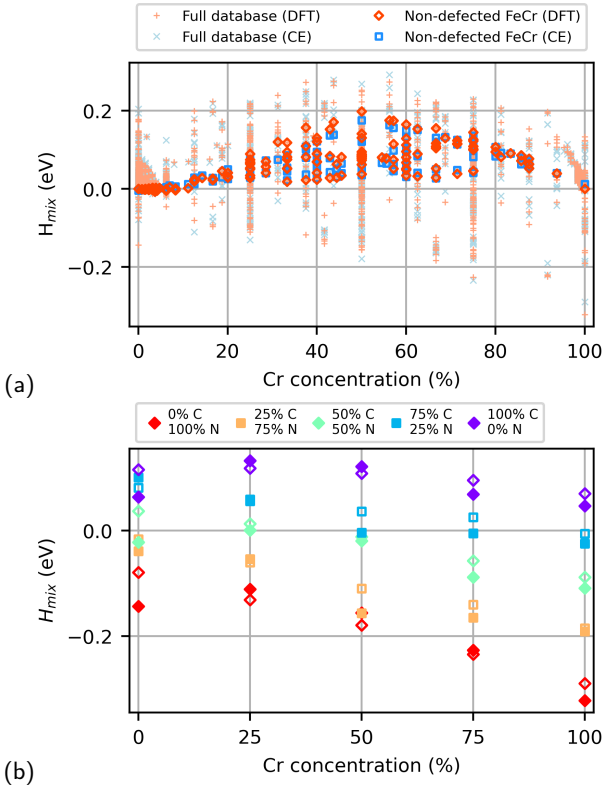

Figure 3: Enthalpies of mixing of various alloy configurations involving the two sublattices. (a) H_{mix} computed using DFT and CE for the entire database, including non-defected structures (bold lines) as well as structures with vacancies, C and N (thin lines). (b) Comparison of mixing enthalpies for α-cementite-type structures $[Fe_xCr_y]_3[C_aN_b]$ obtained from DFT (filled symbols) and CE (open symbols). $[Fe_xCr_y]_3N$ structures are the most stable in the whole of the database.

a chemo-mechanical polish using a suspension of colloidal silica (0.05 um).

3.2. Ion irradiation

Ion irradiation was performed at the laboratory for ion beam interactions in Ruđer Bošković Institute (RBI), Croatia. Both specimens were held using the thermal gradient holder which is described elsewhere [40]. A linear thermal gradient was imposed on across the length of the specimen resulting in a range of irradiation temperatures from 150 to 450 °C. Temperatures were monitored by two thermocouples embedded in one sample and thermal imaging. After the irradiation the cold end and hot end edges were scored with knife to mark the total irradiated area of 14.0×14.5 mm^2. The oval shaped heavy-ion beam (approx. 3 mm wide and 7 mm tall) was rastered over the irradiated area with a frequency of 488 Hz. The defined irradiation area was masked using aluminium plates to monitor the charge in-situ, and the masking was performed on the beam before an electron suppressed Faraday cup which was used to periodically check the beam current for the dosimetry of the exposures. Two irradiations with 4 MeV Fe^{2+} ions were performed, each totalling 3.0×10^{14} ions/cm^2, but one with a total time of 32,900 seconds and the other at a higher dose rate in 6840 seconds. This gave a peak damage of 0.3 dpa, and dose rates of 9.1×10^{-6} (low-dose rate, LDR) and 4.4×10^{-5} dpa/s (high-dose rate HDR). Damage calculations were made using SRIM-2013 using a displacement energy of 40 eV and the "simple" damage calculation method.

3.3. Nanoindentation

A G200 nanoindenter (Keysight, formerly Agilent), with a Berkovich tip was used to perform nanoindentation. Continuous stiffness measurement (CSM) mode was used, with a 2 nm amplitude 45 Hz frequency. The total depth of indentation was 1000 nm to ensure the plastic zone exceeded the irradiated depth and a target strain rate of 0.05/s was used. The tip geometry was calibrated using a fused silica reference sample in accordance with the methodology described elsewhere [41].

3.4. Atom Probe Tomography

A FEI (OR, USA) Helios NanoLab 600i focused ion beam (FIB) was used to prepare atom probe samples from the ion-irradiated material using the lift-out and place on silicon micro-post array method as described elsewhere [42]. Atom probe samples were prepared perpendicular to the surface between 200 and 300 nm in depth, corresponding to an irradiation damage dose of approximately 0.2 dpa.

Atom probe tomography was performed using a Cameca (Ametec, Madison USA) LEAP 5000 XR using a 355 nm UV laser and 52% detection efficiency. The pulse frequency was set to 200 kHz, laser pulse energy of 40 pJ and evaporation rate was kept at 0.005 detected ions per pulse by controlling the voltage. The specimen temperature was held at 50 K. Reconstruction of the atom probe data was performed using IVAS 3.8.4, with an image compression factor of 1.5 and the 0.20 nm spacing of [110] planes was calibrated by changing the initial tip radius in the voltage mode reconstruction method.

The maximum separation clustering algorithm [43] (IVAS 3.8.4) was used with Cr, C and N core ions. In general, a maximum separation, D_{max} of 0.5–0.6 nm with an order parameter [44] of 5 provided good selection of the Cr-dense clusters. The increased order parameter avoided low-density regions of C and N along zone lines. A filter on the number of core ions detected was applied to reduce the chance of including clusters arising from random fluctuations. Depending on the data set, this varied between 35 and 150, to reduce the number of clusters occurring in a randomly mass-relabelled dataset to 100 times less than the number of clusters detected in the original data with the same settings [45]. The inclusion/envelope distance and the erosion distance were both set to half of the D_{max} value.

4. Binding energies of defect clusters

Binding energies of defect clusters of size up to 3 (e.g. 2Vac-1C) were analysed as a part of the assessment of phase stability of Fe-Cr-Vac-C-N alloys. Since our model involves two sublattices, the smallest clusters may be defined either

Figure 4: Binding energies of C-C, N-N and C-N pairs in pure Fe and pure Cr. Negative binding energy indicates repulsion. x-axis is the distance between two impurity atoms in the bcc-octahedral two-sublattice model, illustrated in Fig. 1. Markers give comparison with earlier calculations by [a] Barouh *et al.* [17] and [b] Domain *et al.* [14].

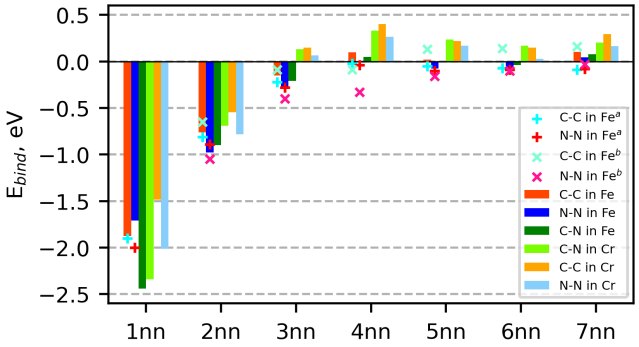

on the same sublattice, i.e. as a bcc-bcc defect cluster or as an octahedral-octahedral defect cluster, as well as an inter-sublattice bcc-octahedral defect cluster.

4.1. Binding in 2-body clusters

4.1.1. Binding between interstitial atoms, and interstitial atoms and vacancies

To rationalise why the locations of the regions with higher Cr concentration in Fe-Cr alloys observed experimentally correlate with the locations of higher concentration of C and N impurities, the binding energies of C-C, N-N and C-N impurity two-body clusters in Cr and Fe matrices were investigated and compared with literature data.

Fig. 4 and Table 1 show that at smaller distances, the strength of repulsion between the impurity atoms is high, corresponding to large negative binding energy. Interaction between interstitial impurities weakens as the distance between the interstitial atoms increases, in agreement with the data given in Refs. [14, 17]. The binding energy for all the two-body impurity clusters becomes positive in Cr matrix starting from the 3nn distance, implying attraction, compared to the Fe matrix where attraction starts from the 4nn distance. Interaction between impurities is stronger in Cr than in Fe. We also find that the N-N (nitrogen-nitrogen) interaction is always weaker compared to C-C interaction, except for the case of a N-N pair in Fe matrix at the 1nn distance. The smallest distances between the interstitial impurities in the structure of a bcc-precursor of α-cementite are 5nn and 6nn, and the binding energies at those distances are positive in the Cr matrix, but are slightly negative or close to zero in the Fe matrix. This suggests that C and N may form cementite-type clusters, and this trend is slightly stronger pronounced in the Cr matrix. The formation of structures with other type of ordering (e.g. with the shortest distances between interstitial atoms being 4nn and 7nn) might be more preferable.

Figure 5: Binding energies of Vac-Vac clusters in Fe and Cr, shown together with the binding energies of Vac-Cr and Cr-Cr clusters in Fe as a function of a distance between Cr atoms, in bcc nearest neighbour units. Literature values are taken from [c] Domain et al. [48], [d] Lavrentiev et al. [18], [e] Bakaev et al. [49].

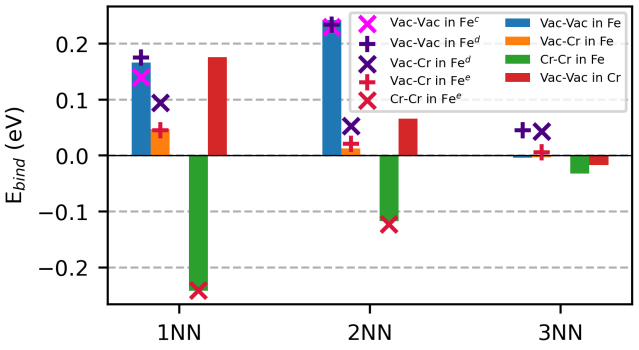

4.1.2. Binding in the bcc sublattice

It is important to investigate interaction between Cr atoms in a non-defective Fe matrix to see if Cr exhibits any tendency towards precipitation in the absence of C or N impurities or vacancies. Fig. 5 shows that Cr atoms in bcc Fe matrix repel each other, with repulsive interaction being the strongest at the 1NN distance, rapidly decreasing as a function of distance between Cr atoms. At the 3NN distance the interaction is 8 times weaker than at the 1NN distance, still remaining repulsive. The values shown in Table 2 illustrate that Cr-Cr interaction remains repulsive at the 5NN distance. This agrees with the data from Refs. [46, 47].

Since vacancies form in abundance under irradiation, their effect on Cr clustering also warrants investigation. Two vacancies form what is known as a divacancy, referred to below as Vac-Vac. Vacancies bind at 1NN and 2NN distances in bcc Fe and Cr matrices and this binding quickly diminishes as a function of distance between the vacancies, see Fig. 5. Binding between vacancies in bcc Fe is stronger than in bcc Cr, and this can make vacancies stay in the Fe-rich part of the lattice. In bcc Fe matrix the Vac-Vac binding energy is higher at 2NN than at 1NN distance, and this is reversed in bcc Cr. Moreover, interaction between vacancies in Cr at the 3NN distance is repulsive. Vacancies bind to Cr much weaker than to each other ($\sim$ 0.05 eV versus $\sim$ 0.18 eV), and at the 3NN distance Vac-Cr clusters already start exhibiting slight repulsion, see Fig. 5. This suggests that vacancies are not expected to facilitate clustering of Cr and instead the evolution of vacancies gives rise to the formation of vacancy clusters or voids. Binding energies of Vac-Vac, Vac-Cr and Cr-Cr clusters are generally in agreement with the literature values taken from Refs. [48, 49, 18], see Table 2.

4.1.3. Binding of interstitial atoms to vacancies

We now consider interaction between interstitial C and N atoms with vacancies. Vac-C and Vac-N clusters form bound configurations in Fe and Cr matrices, with stronger attraction found in Cr, see Fig. 6. This agrees with the analysis performed in [17, 14]. Vac-N binding is always stronger

Table 1
Binding energies computed for C-C, N-N and C-N clusters in pure Fe and pure Cr. Distances are given in the notations of the bcc-octahedral two-sublattice model, illustrated in Fig. 1. Literature values from Barouh *et al.* [17] and Domain *et al.* [14] are also shown for comparison.

Dist. [nn]	2C in Fe [eV]	2N in Fe [eV]	CN in Fe [eV]	CN in Cr [eV]	2C in Cr [eV]	2N in Cr [eV]
1	-1.874 -1.9 [17]	-1.710 -2 [17]	-2.441	-2.345	-1.484	-2.014
2	-0.762 -0.81 [17] -0.65 [14]	-0.976 -0.89 [17] -1.05 [14]	-0.897	-0.693	-0.544	-0.784
3	-0.149 -0.22 [17] -0.09 [14]	-0.272 -0.28 [17] -0.4 [14]	-0.215	0.132	0.148	0.065
4	0.098 -0.02 [17] -0.09 [14]	-0.005 -0.04 [17] -0.33 [14]	0.049	0.331	0.403	0.264
5	0.019 -0.05 [17] 0.13 [14]	-0.077 -0.1 [17] -0.16 [14]	-0.004	0.237	0.220	0.168
6	-0.004 -0.07 [17] 0.14 [14]	-0.093 -0.09 [17] -0.1 [14]	-0.041	0.169	0.147	0.029
7	0.103 -0.09 [17] 0.16 [14]	0.045 -0.08 [17] -0.03 [14]	0.077	0.202	0.295	0.166

Table 2
Binding energies computed for two-body interstitial defect clusters in Fe and Cr as a function of distance between the atoms, expressed in bcc nearest neighbour units. Literature values are from Domain *et al.* [48], Bakaev *et al.* [49], and Lavrentiev *et al.* [18].

Distance [NN]	Vac-Vac in Cr [eV]	Vac-Vac in Fe [eV]	Vac-Fe in Cr [eV]	Vac-Cr in Fe [eV]	Fe-Fe in Cr [eV]	Cr-Cr in Fe [eV]
1	0.176	0.166 0.14 [48] 0.175 [18]	-0.870	0.047 0.045 [49] 0.094 [18]	-1.122	-0.242 -0.241 [49]
2	0.066	0.242 0.23 [48] 0.234 [18]	-1.008	0.013 0.021 [49] 0.053 [18]	-1.407	-0.117 -0.123 [49]
3	-0.017	-0.004 0.045 [18]	-1.074	-0.003 0.006 [49] 0.043 [18]	-1.287	-0.032
4	-0.808	0.064 0.055 [18]	-1.133	-0.011 -0.016 [49] -0.01 [18]	-1.439	-0.034
5	-0.913	0.071	-1.052	0.028 -0.001 [18]	-1.264	-0.033

than binding in Vac-C except for the case of the 6nn configuration. The energy of binding between a vacancy and an interstitial atom is minimum at the 5nn distance.

Binding energies computed for the C-C, N-N, Vac-C and Vac-N clusters are generally in agreement with literature data [17, 21].

Fig. 6 also shows binding energies of Cr-C and Cr-N configurations. All the binding energies are negative, indicating repulsion; at the 1nn and 2nn distances Cr-N binding is less negative compared to Cr-C, and at the 5nn and 6nn distances the sign is reversed. The data on Cr-C binding agree very well with the data published in Ref. [49].

4.2. Binding in 3-body clusters

Since 3-body interactions are taken into account in our CE model, it is necessary to analyze binding energies of 3-body defect clusters, more specifically, mixed bcc-oct clusters.

Table 3
Binding energies of Vac-C and Vac-N clusters in pure Fe and pure Cr shown as a function of the distance between a vacancy and an impurity. Literature values are taken from Barouh *et al.* [17], Bakaev *et al.* [49], Domain *et al.* [14].

Distance	Vac-C in Fe	Vac-N in Fe	Vac-C in Cr	Vac-N in Cr	Cr-C in Fe	Cr-N in Fe
[nn]	[eV]	[eV]	[eV]	[eV]	[eV]	[eV]
1	0.598 0.41 [17] 0.47 [14]	0.866 0.73 [17] 0.71 [14]	1.551	1.592	-0.241 -0.214 [49]	0.006
2	0.053 -0.16 [17] -0.01 [14]	0.276 0.17 [17] 0.2 [14]	0.515	0.532	-0.228 -0.23 [49]	-0.114
5	0.039 -0.08 [17]	0.084 -0.01 [17]	0.247	0.307	-0.079 -0.088 [49]	-0.103
6	0.257 0.18 [17]	0.238 0.18 [17]	0.460	0.350	-0.042 -0.048 [49]	-0.056
8	-0.031 -0.04 [17]	-0.049 -0.06 [17]	0.063	0.041	-0.028 -0.046 [49]	-0.037
9	-0.022	-0.007	0.022	0.021	-0.022	-0.028

Figure 6: Binding energies of Vac-C and Vac-N clusters in pure Fe and pure Cr, and binding energies of Cr-C and Cr-N clusters in pure Fe, shown as a function of the distance between a vacancy and an impurity atom. At distances of 3nn, 4nn and 7nn there are no 2-body clusters involving atoms residing on different sublattices, hence such distances are not shown on the x-axis of the graph. Reference values are taken from [a] Barouh et al. [17], [b] Domain et al. [14], Bakaev et al. [49].

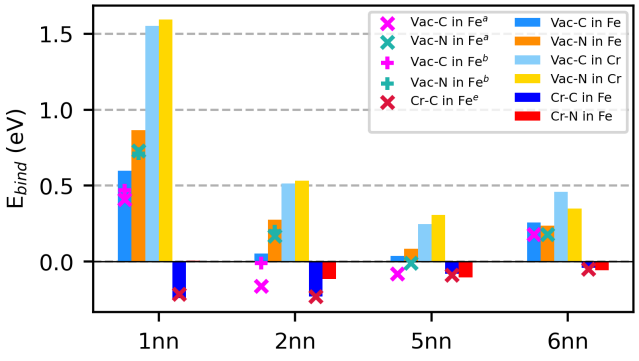

Figure 7: Binding energies of clusters containing one vacancy and two interstitial atoms in Fe. The notations on the horizontal axis are as follows: the first two digits in a label represent the distance between each impurity atom and a vacancy, and the third digit refers to the distance between the impurities. For example, a 112 configuration corresponds to the occupied sites 0,1,1 in Fig. 1. Reference values are taken from [a] Domain *et. al* [14] and [b] Bonny *et. al* [19].

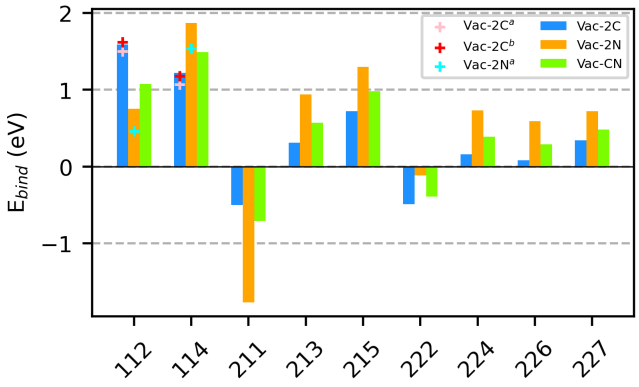

4.2.1. Binding of two interstitial atoms to a vacancy

Defect clusters involving one vacancy and two interstitial atoms, carbon or nitrogen, bind together when the distance between the interstitial atoms is larger than their distances to a vacancy. They exhibit repulsion when the distance between the interstitial atoms is smaller or equals to the distance between them and the vacancy, see Fig. 7. The notations used for the horizontal axis in Fig. 7 are as follows: the first two digits in a label give information about the distance between a vacancy and each impurity atom, the third digit is the distance between the impurities. For the case of a Vac-CN, there are configurations where either C or N is closer to a vacancy. The difference between the binding energies of such clusters is quite small and only a cluster with higher E_{bind} is shown in the figure. Binding energies derived from our calculations are in agreement with literature data [14, 19].

4.2.2. Binding of 2 vacancies to an interstitial atom

A number of 3-body clusters involving 2Vac and C or N, considered by Barouh *et al.* [17] in the context of bcc Fe matrix were also explored for bcc Cr. The binding energies computed for those clusters are shown in Fig. 8. The magnitude of attraction is higher in a 2Vac-1N cluster than in a 2Vac-1C cluster, in the bcc Fe environment. In bcc Cr, there is no clear difference between the two types of clusters, but for both cases the binding is stronger compared to their counterparts in bcc Fe. Similarly to the case of the two-body vacancy-impurity clusters, the positive binding energies of the clusters might be responsible for the formation of 2Vac-C/N clusters in Fe-Cr-Vac-C-N alloys, with possible slight

Figure 8: Binding energies of 2Vac-C and 2Vac-N clusters in pure Fe and pure Cr. The notations are as follows: the first two digits in a label give information about the distance between each vacancy and the impurity atom, and the third digit refers to the Vac-Vac distance.

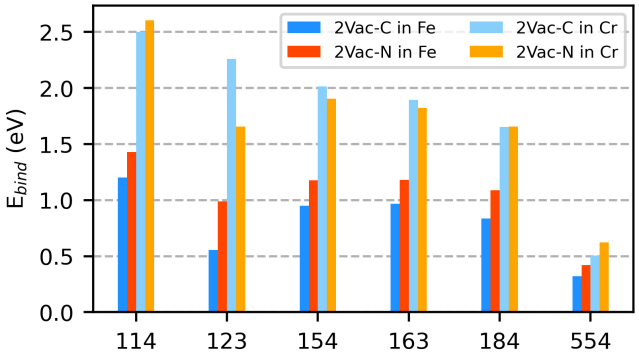

preference of them forming in the Cr-enriched regions.

4.3. Overview of binding energies

From the analysis of binding energies above, we observe that interstitial atoms attract at large distances but prefer not to stay too close to each other. This type of interaction favours the formation of structures with increased yet relatively disperse distribution of interstitial atoms, for example ordered phases similar to α-cementite-like structures. The addition of vacancies may modify the behavior of interstitials, and the strong attraction between vacancies and interstitials may overcome the repulsion of interstitials at short distances, promoting the segregation of interstitial impurities to vacancies. Since vacancies attract at the nearest and next-nearest neighbour distances, the above pattern of interaction favours the formation of voids surrounded by carbon and nitrogen atmospheres.

Cr-Cr repulsion is stronger than Cr-Vac attraction. Cr-interstitial clusters also have negative binding energies, i.e. Cr solute atoms and interstitial impurities repel each other, resulting in that the formation of Cr-C/N clusters appears unlikely. We note that this does not agree with the earlier analysis of α-cementite-like structures in Fig. 3(b), suggesting that $Cr_3[N_xC_{1-x}]$ structures have negative formation energy and hence are expected to be stable. This contradiction may be explained by the fact that the two observations involved different choices of the reference environment: binding in 2-atom clusters was investigated in pure metals, whereas the analysis of α-cementite-like structures spans mixed matrices and significantly higher concentrations of interstitial impurities.

5. Monte Carlo simulations

Interactions in a Fe-Cr-Vac-C-N alloy are complex and vary significantly, depending on the local composition of the alloy. To explore effects of segregation in irradiated Fe-Cr alloys, we performed MC simulations of Fe-Cr-Vac-C-N alloys containing 3.28 at. % Cr at 650 K. This corresponds to the alloy composition and irradiation temperature used for the experimental observations described in Section 3. MC simulations assess the thermodynamic equilibrium state of an alloy at a given temperature.

In what follows, we explore the effect of interstitial C and N atoms as well as vacancies on the microstructure of Fe-Cr alloys.

5.1. The role of interstitial impurity atoms in alloys without vacancies

The effect of C and N impurity atoms on the phase stability of Fe-Cr-C-N alloys containing no vacancies is shown in Fig. 9(a). In an alloy containing no C and N impurities (see the left panel in Fig. 9(a)), the Cr atoms, shown as grey points, are uniformly distributed over the lattice, in agreement with earlier theoretical and experimental studies [46, 50].

If C and N interstitial atoms are present in the system, usually they are not distributed randomly throughout a supercell, but form locally ordered phases, starting from concentrations as small as 0.02 at. % (see Fig. 9(a), middle and right panels). The types of clusters most observed for equal concentrations of C and N in an alloy without vacancies are shown in Figs. 10(g) and Figs. 10(h), which are locally ordered [Fe,Cr][N,C] and [Fe,Cr]N clusters, respectively. The ratio of Cr to Fe content in such clusters may vary, but generally with the increasing concentration of C and/or N in a cluster, the concentration of Fe in a cluster decreases and the concentration of Cr increases both for Fig. 10(g) and (h) types of clusters. The concentration of Cr is higher on average in clusters of type Fig. 10(h), which contain more N, compared to Fig. 10(g).

In clusters of type Fig. 10(g), C and N impurities prefer to group to the impurities of the same type on the interstitial sublattice. This results either in the formation of a cluster which is an agglomerate of two parts, with a high concentration of C or N in either part (as seen in Fig. 10(g)), or, more rarely, in the formation of a cluster where one impurity type aggregates in the inner part, and the other in the outer part of the cluster. Fe atoms are observed more often in the C-rich part of the cluster. In clusters of Fig. 10(h) type, Fe atoms are observed only at clusters' boundaries.

5.2. The role of vacancies

The effect of vacancies on the microstructure of Fe-Cr-C-N alloys is shown in Fig. 9(b). The concentration of vacancies in the structures generated using MC simulations was 0.005 at. %.

First, we note that vacancies do not form clusters in Fe-3.28%Cr alloy at 650 K if there are no impurities present in the material (see the top left panel in Fig. 9(b)).

The effect of vacancies on the clustering of interstitial impurities is noticeable and is different for C and N interstitials. Nitrogen prefers to occupy the nearest neighbourhood of any amount of vacancies, even one, which leads to the formation of multiple of such defect clusters in the simulated cell (see Fig. 9(b) middle left). This type of cluster, shown in Fig. 10(a), is the smallest one observed throughout all Monte Carlo simulations.

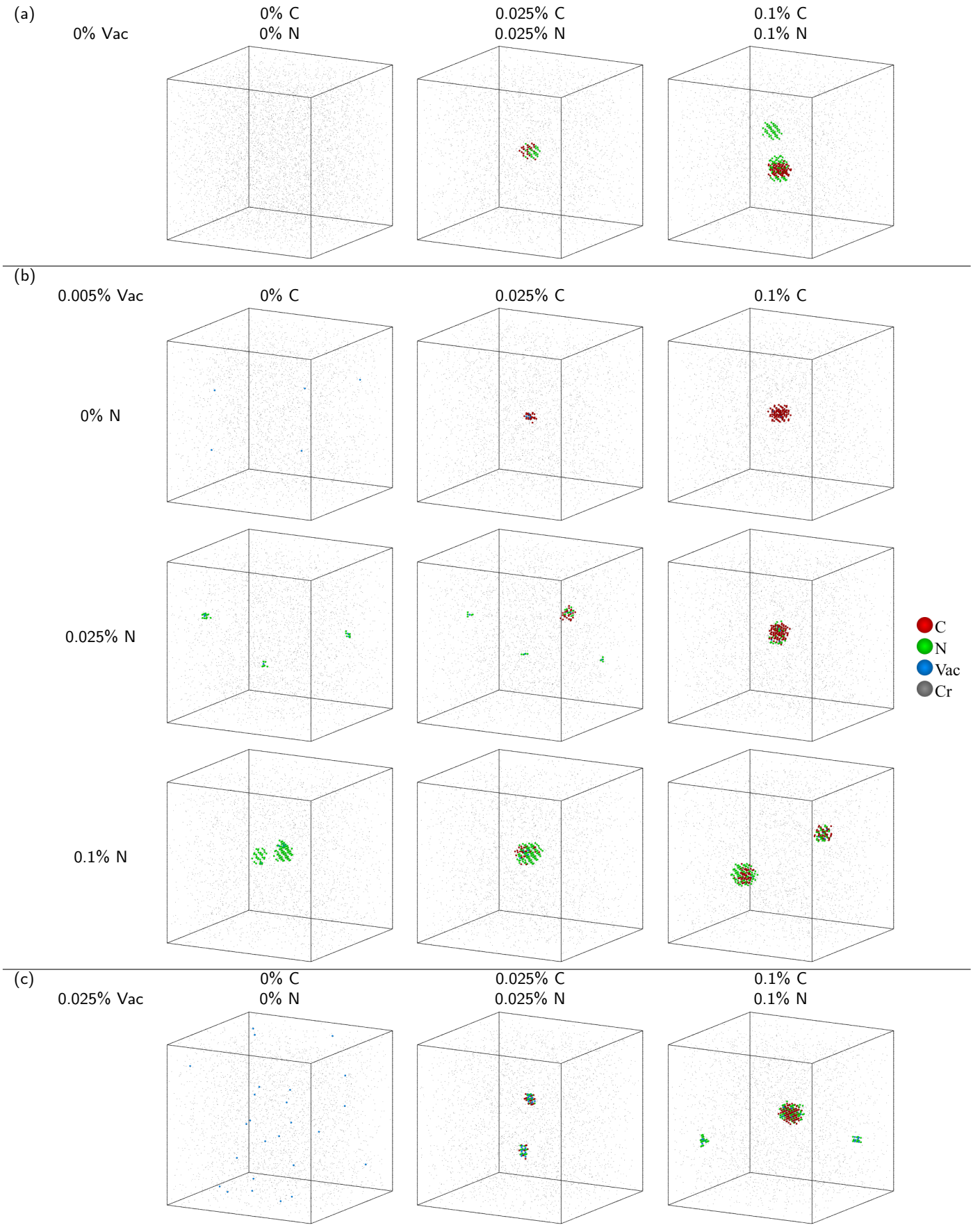

Figure 9: Monte Carlo snapshots comparing Fe-3.28%Cr with varying concentrations of C and N at 650 K for vacancy concentrations (a) 0%, (b) 0.005% and (c) 0.025%.

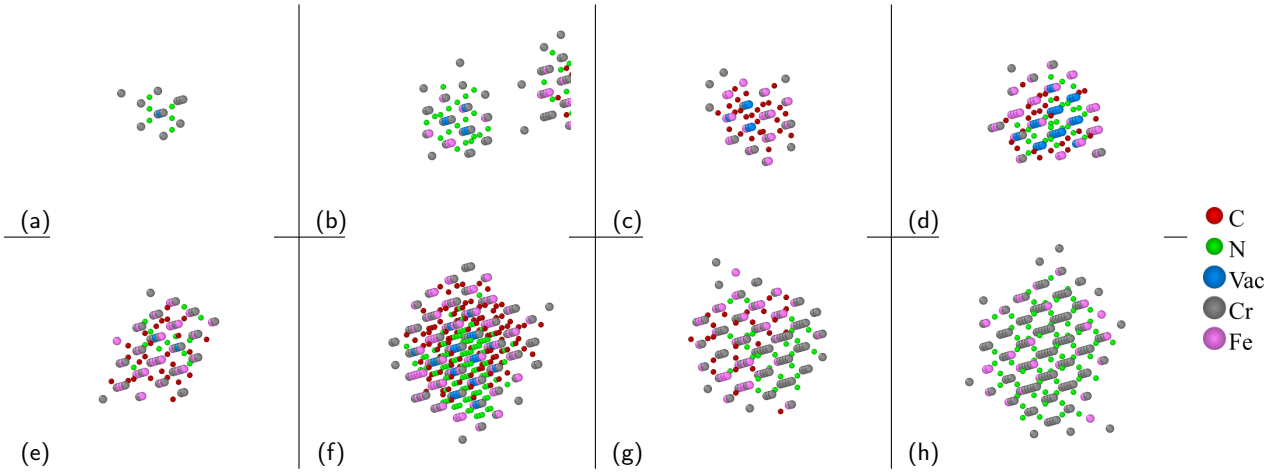

Figure 10: Most observed clusters in compositions presented in Fig. 9, which are various combinations of vacancy concentration equal to 0, 0.005 and 0.025 % and concentration of C and N equal to 0, 0.025 and 0.1 %. The average size increases from (a) to (h).

With higher N concentration (Fig. 9(b), bottom left) the defects aggregate together and form bigger clusters with N and vacancies (Fig. 10(b)) observed in smaller numbers in the supercell, compared to the lower N content.

Carbon does not form small clusters and instead usually forms one big cluster of type Fig. 10(c) in the simulated cell, which increases in size with increasing C concentration (see Fig. 9(b) top row).

For identical nominal concentrations of C and N, when their total concentration does not exceed approximately ten times the vacancies concentration (Fig. 9(b) center), there can be observed smallest Vac-N clusters of type Fig. 10(a) and a new type of cluster – mixed C-N-Vac with C concentration being slightly higher than N, shown in Fig. 10(e). All C in the supercell is found in this type of cluster at nominal composition presented in (Fig. 9(b) center).

With increasing C+N concentration above ten times that of vacancies, only the clusters of type Fig. 10(e) are observed in the lattice and multiple of such with high C+N concentration (see Fig. 9, bottom right).

5.3. Effect of higher vacancy content

The microstructure of Fe-3.28%Cr alloys containing C and N impurities and a higher concentration of vacancies, namely 0.025 %, is shown in Fig. 9(c). In supercells without C or N, the vacancies are distributed uniformly in the lattice (see Fig. 9(c), left panel).

For the concentration of C+N, being 2 times higher than that of Vac (Fig. 9(c), middle), we observe predominantly the clusters of type Fig. 10(d). This type is similar to Fig. 10(e) in that it has all elements considered in the simulations, however, Fig. 10(d) type has Vac and Fe dominantly on the bcc sublattice instead of Cr, which is dominant in Fig. 10(e) type clusters.

Since the interstitial sublattice has 3 times more positions than the bcc sublattice, it may be assumed as a theoretical threshold value in MC simulations when the interstitial sublattice part of the bcc Vac cluster is completely filled with C and/or N. Below this limit, the interstitials can be described as situated inside the void. It should be noted that since the MC simulation model used in this study uses a rigid lattice, the actual distorted configuration of a defect cluster with C and/or N inside the void remains effectively unknown. In a real alloy, the formation of C+Vac clusters might result in the precipitation of graphite, whereas N+Vac clusters probably form gas bubbles, i.e. small voids filled with N_2 molecules.

In Fig. 9(c), right panel, the ratio of C+N to Vac is higher than the aforementioned threshold value, which leads to the occurrence of clusters of type Fig. 10(f), where the concentration of Cr, although not dominant, is increased compared to nominal Cr concentration. C atoms are mostly found in those types of clusters, and N can also be found in multiple small clusters of type Fig. 10(b) throughout the supercell.

It should be mentioned that voids containing no interstitial atoms have been observed only in the simulations with nominal vacancy concentrations approaching and higher than 0.1% and resembling a material exposed to a high dose of irradiation [10, 51], although in majority of simulations with such Vac concentrations the vacancies have been still most likely distributed uniformly throughout the supercell.

5.4. Summary of Cr clustering as a function of C, N and vacancy concentrations

Fig. 11 presents the analysis of Cr concentration around interstitial defects. The maximum separation distance for the detection of clusters where the concentration is calculated, is the same as in APT and MC analysis, and is equal to 0.4 nm. Due to the lattice nature of MC simulations, the maximum separation distance there is effectively limited to 0.347 nm = 6nn = 2NN – the largest bcc-oct distance considered in the model.

As can be seen in Fig. 11, there is a strong correlation of Cr concentration around interstitial defects with both the

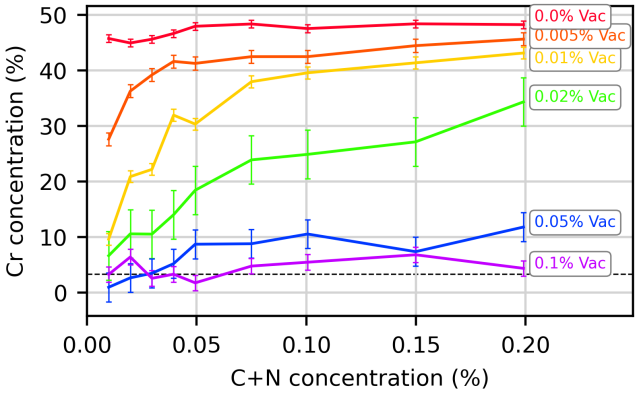

Figure 11: Concentration of Cr in Cr-C-N-enriched clusters at 650 K. The concentration is calculated using the method of maximum separation distance with the following parameters: $d_{max} = d_{bulk} = d_{erode} = 0.4$nm, $n_{min} = 10$. Concentrations of C and N are equal, %C=%N=%(C+N)/2. Series represent different nominal concentrations of vacancies in the alloy. All the data points in the series represent values averaged over 10 simulations with identical parameters, starting from different random initial positions of atoms. Error bars around each point show confidence intervals with α=0.95. Dashed line indicates nominal concentration of Cr in all simulations, 3.28 at.%.

concentration of vacancies and the interstitial defects themselves, although the correlation is different in sign. For any concentration of vacancies, the Cr concentration increases with the increase of C+N concentration – Cr tends to precipitate around the interstitial defects. The largest concentrations are observed when there are no vacancies in the alloy and with the concentration of interstitials as low as 0.01%. When vacancies are added to the alloy, Cr concentration around the defects decreases, and this reduction is more pronounced at higher concentration of vacancies. This is caused by the formation of voids and aggregation of C/N interstitials inside these voids instead of the formation of ordered phases involving Cr. As can be seen in the figure, the concentration of Cr does not exceed the nominal concentration when %Vac = %C+N. To make sure that the observed increased Cr concentration is not caused by the poor choice of the cutoff, larger cutoff of 0.53 nm = 14nn = 6NN has been tested and the increased concentration of Cr around interstitial defects is still observed, with the effect being on average 5% smaller compared to the 6nn cutoff.

6. Experimental results from APT

Atom probe tomography revealed a high number density of Cr-rich clusters in the Fe-3.28Cr material irradiated with the high and low dose rates. Fig. 12 shows a representative 65x65x65 nm^3 volume and the clusters which have been detected. Across all samples, the mean cluster number density was 2.4–6.3×10^{22} clusters per m^3 (95% confidence interval, CI95%), as defined by the cluster selection parameters given in the methods section.

Note that these Cr-rich regions, Fig. 12a, also correlate with increased C and N contents, shown separately in Fig. 12b. The initial C and N content is very low, less than 8 ppm in total, however in the irradiated samples the measured content of C and N was 42±5 and 151±3 atomic ppm (8 experiments totalling 116 million ranged ions, 2 volumes with excess C near the original tip surface were excluded). The excess solute measured is likely to be the result of contamination from the ion beam irradiation, which is commonly observed [52].

Several clusters were observed as being coherent along the [110] direction and so it is expected that these clusters are at least semi-coherent with the BCC lattice. The atom probe data have been reconstructed to give accurate plane spacings in the matrix, however there is evidence of trajectory aberrations in the vicinity of the clusters which makes direct measurement of their size uncertain. Measuring the cluster diameter parallel to the analysis direction should give the most reliable measurement [53], and this was measured as 2.7–3.1 nm CI95%.

To give a reproducible indication of size irrespective of reconstruction parameters, the excess Cr ions can be counted using the "matrix correction" described in Ref. [45]. Excess ions are measured after removing all the Fe ions and the corresponding proportion of Cr according to the expected matrix composition. The clusters had a detected range of excess Cr ions between 100 and 130 (CI95%). A known fraction of ions are lost in the evaporation and detection process, however after correcting for the detector efficiency, the clusters are expected to contain 190–250 excess Cr ions (CI95%).

The composition results from the maximum separation method, no overlap solving or background subtraction, gives the average composition of individual clusters. The 95% confidence interval for the cluster composition was Fe 50.5–51.9%, Cr 45.2–46.8%, C 0.24–0.38% and N 2.0–2.8% all in atomic percent.

To test the reliability of the cluster selection parameters, the variability of reported results were investigated with a range of D_{max} values. Analysis of the same data set with similar D_{max} values of 0.50, 0.55 and 0.60, with the inclusion and erosion distances set to $D_{max}/2$, gave Cr fractions in the clusters of 0.48, 0.47 and 0.45 all with approximately ±0.05 95% confidence intervals. While the clusters identified did not change, their apparent concentration is somewhat sensitive to the inclusion and erosion parameters selected.

The analysis of the Cr-rich clusters by atom probe is complicated by a number of factors. These are broadly separated into two groups, relating to the spatial location of ions and to the measured composition. The small size of the clusters, containing only a few hundred excess Cr ions, is approaching the limit of what can be reliably be separated using cluster detection. This will increase the subjectivity of the analysis and the accuracy of the measured composition.

The increased reconstructed density in the vicinity of the clusters is evidence of some de-magnification during evaporation and the resulting trajectory aberrations will reduce the accuracy of the spatial reconstruction, thus impacting the selection of the clusters.

Without other supporting evidence, it is not possible to

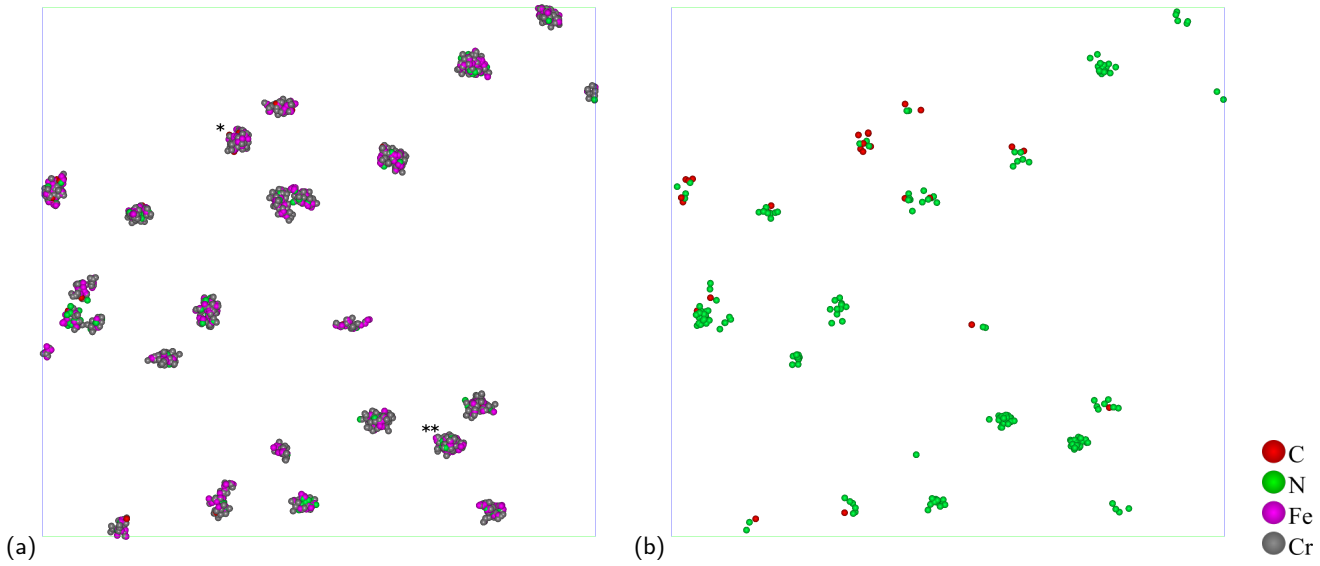

Figure 12: Clusters in experimental data isolated from their surroundings in Fe-3.28%Cr alloy. A variation in C and N content is observed. Figure size is 65x65 nm. a) showing Fe, Cr, C and N, b) showing only C and N. Average cluster composition: Fe-50.4 Cr-44.1 N-4.7 C-0.7 at%. * and ** indicate clusters shown in detail in another figure.

tell reliably using atom probe what fraction of Fe is a true component of the clusters and that which is included by the cluster selection and trajectory aberrations. From looking at a range of reasonable cluster selection parameters, the Cr fraction is in the range of 0.3 to 0.6.

Turning to the C and N concentration in the clusters, this is likely to be effected by several artefacts which reduce the measured impurity content. Thermally activated surface migration of some species is enhanced by the electric field and may cause C and N to migrate from the clusters before evaporating [54]. There is some evidence of the mobility of these ions from the clusters by looking at volumes of the data with and without clusters. Volumes with clusters, but with the clustered ions removed, showed an 80% increased content of C and N, from 70±40 to 120±40 and from 130±20 to 230±30 atomic ppm respectively, as compared to a volume which did not contain any detected clusters. This increase in solute in the region surrounding the clusters suggests some migration of these ions from the clusters meaning they are not included in the cluster selection and subsequent measurement. Based on the concentration of C and N, in volume around the clusters contained 125 extra C ions and 230 extra N ions, compared to 19 C ions and 35 N ions detected in the clusters themselves. C and N are either lost from the cluster or there is extra C and N near where the clusters are because of other microstructural features like dislocations.

Using the cluster radial concentration profile in IVAS the Cr concentration was enhanced to a distance of 2–2.5 nm from the cluster center but the C and N concentration was increased up to a distance of 4–6 nm. The composition of a radius of 6 nm around the cluster centers (with the cluster ions removed) had an increased C and N content of $40 < C = 100 < 170$ and $260 < N = 320 < 380$ compared to $10 < C = 17 < 26$ and $89 < N = 97 < 103$ atomic ppm in the remainder of the analysis volume more than 6 nm from any cluster. In these 6 nm radius spheres, this is an excess of 75 C atoms and 204 N atoms, after background subtraction and correcting for detection efficiency, compared to 19 C and 244 N atoms detected as part of the cluster selection. If these excess solute atoms all are associated with the clusters, it means that the clusters only account for 20% of the C and 45% of the N solute atoms which are actually increased in the region of the clusters. To "correct" the solute content of the cluster composition by MSM the C content would be multiplied by 5 and the N content doubled, with other loss mechanisms ignored.

The atom probe data measurements show some microstructural features, including small dislocation loops and dislocation lines which are highlighted by a slight segregation of Cr. The detected dislocation lines had a total length of 155 nm in a volume of 0.003 um^3, a density of 5.3×10^{-5} nm^{-2}. Five dislocation loops were detected with a mean diameter of 7±4 nm (CI95) and number density of 1.7×10^{21} m^3. This analysis includes 171 Cr-rich clusters which are not obviously associated with dislocations or dislocation loops. The approximate total volume fraction of the microstructural features was 0.2%, 0.8% and 1.0% for the clusters, loops and dislocation lines respectively. The distribution of solute between these different features was quantified, with background subtraction and overlap solving, by placing spherical volumes around clusters, with a radius equal to the cluster radius, and around dislocation loops, with a radius slightly bigger than the observed Cr segregation. The composition around dislocation lines was quantified in a similar manner but using 5 nm radius cylinders oriented along the Cr-segregated regions. A summary of the distribution of the solute in the different microstructural features is shown in Fig. 13. The solute in these features represents 0.4% of all Cr, 6.5% of all

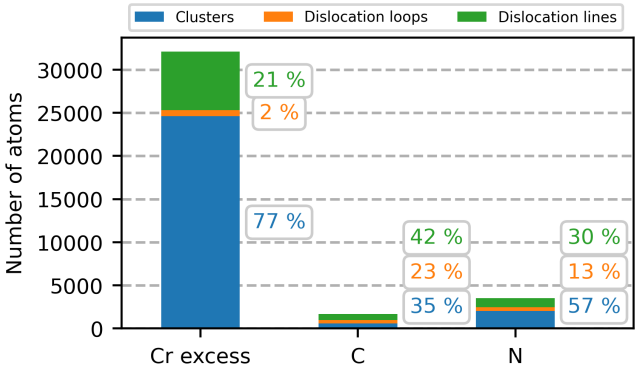

Figure 13: APT analysis showing the absolute distribution of solute between three microstructural features (clusters, dislocation loops and dislocation lines) in the irradiated Fe-3.28%Cr alloy samples with the presence of the carbon and nitrogen impurities. The count of Cr here refers to the excess Cr in these features, whereas for C and N these are the absolute counts. Relative distribution for each element is shown as percentage on the right of corresponding bars.

C and 10% of all N detected. Of the segregated solute, 77% of Cr was in the clusters and the remainder was primarily in dislocation lines. Because most of the segregated Cr is in the clusters, it is reasonable to assume the Cr behaviour in these samples is dominated by the cluster formation. By comparison less of the segregated C and N is partitioned into the clusters, only 35% and 57% respectively. Therefore Fig. 13 indicates there are differences in the behaviour of C and N in this alloy system, specifically that N has a stronger preference to segregate to the Cr-rich clusters than C does.

Another factor which potentially effects the measured C and N composition is the non-detection of multiple hits due to limitations of the delay line detector used in the atom probe technique [55]. To decide if this multiple hit loss is occurring, we can investigate the detected multiple hits for inconsistencies.

Matrix C-content multiples are 30%, but in the clusters multiples comprise 90% of the detected C ions. For nitrogen there is a higher multiples fraction of detected multiples in the matrix (48% are multiples) than the clusters which have a 12% multiple composition. Note that there are approximately ten times as many detected N ions than C ions. For reference there are 9% multiples of Cr in the matrix and 13% in the clusters. Multiple hit loss is more likely where there are a higher fraction of multiples, therefore this evidence points towards likely loss of carbon from the clusters. For nitrogen, the lower multiple fraction in the clusters compared to the matrix may be due to the majority of the matrix-N evaporating from zone-lines and the associated evaporation physics. There is almost 50 times as much N measured at the 110 pole than a non-pole volume, and only 4 times as much C comparing the same volumes. However, the lower measured multiple fraction might indicate that some of the N ions are not detected due to multiple-hit loss.

In summary, a high number density of small Cr-rich clusters were detected in both Cr concentration materials in both irradiation conditions. These clusters were small (2.9±0.2 nm) with a Cr-fraction of 0.3–0.6, C+N fraction of 0.05 and some evidence of loss of C and N from the measured cluster composition.

7. Comparison of simulations with experimental observations

For the analysis of both experimental samples and the Monte Carlo simulations, Maximum Separation Method has been chosen, which is described elsewhere [56].

It has been shown that there is a variety of observed types of clusters in Fe-Cr-Vac-C-N alloys both in MC simulations (see Fig. 10) and APT measurements (see Fig. 12).

Fig. 14 shows pairs of example clusters from APT observations and MC simulations to illustrate the difference in the structure of clusters between the simulations and observations. As can be seen from the figure, the APT clusters are less dense and larger in size compared to MC clusters: average size of clusters in APT is 2.9 nm, whereas it is 0.9 nm in MC simulations. This is attributed to the trajectory aberrations that smears the positions of atoms in the directions perpendicular to the evaporation direction. The number of interstitials found inside the cluster is also much smaller in APT compared to MC simulation, which can be caused by the multiple-hit loss of C and N in the experiment, whereas all atoms are tracked in the simulations. Both these factors result in the lower density of the cluster in APT measurements in comparison with MC simulations. On the other hand, the structure of MC simulations is not completely representative due to on-lattice nature, which does not show the changes to the structure caused by the stress fields of the defects.

Since APT does not detect vacancies, only C, N and Cr density in the clusters may be compared. It should be noted that Monte Carlo simulations produce the atomic arrangement at thermodynamic equilibrium, which may not be fully established in the experimental samples. The experimental measurements are not expected to be at thermal equilibrium due to the influence of the ion irradiation, which causes additional displacement mixing, and the short duration (several hours) of the irradiation exposure. As has been discussed in Section 6, the interstitial elements are found not only inside the clusters, but also in the close vicinity of the clusters, showing the tendency of Cr and interstitials to aggregate together. It can be hypothesized, that this is the off-thermal equilibrium state, and given enough thermal energy, the interstitials would migrate inside the clusters forming structures similar to ones observed in MC simulations.

A set of MC simulations with the nominal concentrations of defects identical to those in experimental sample has been performed. Since the vacancy concentration in the experimental samples is not known, only their presence is certain, two additional sets of simulations have been performed with various Vac concentrations (0.005 at.% and 0.01 at.%). The results of these three sets of simulations are compared to the results of experimental measurements in Fig 15. As can

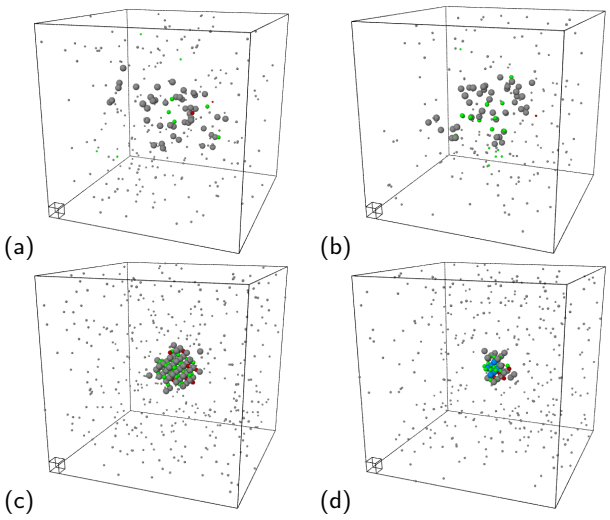

Figure 14: Visual comparison of example clusters found in (a-b) APT experimental measurements and (c-d) MC simulations. Unit cell of 0.28 nm size is shown in the left near corner of each subfigure. (c) is taken from a simulation without vacancies and Fe-3.28at.%Cr, 0.007at.%C + 0.028at.%N, (d) is taken from Fe-3.28Cr, 0.01at.%Vac, 0.007at.%C + 0.028at.%N.

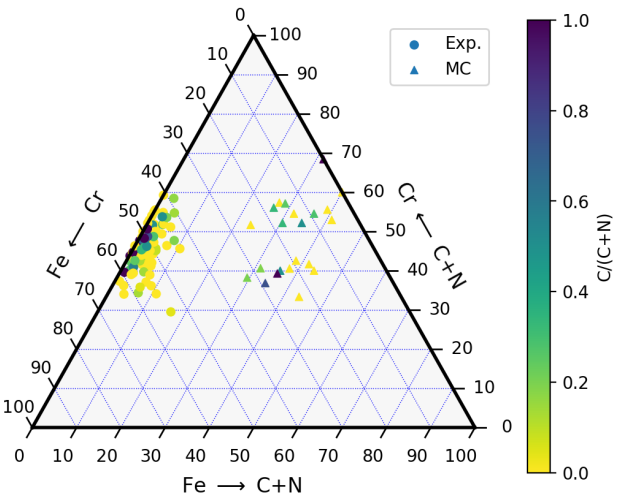

Figure 15: Relative concentration of Cr,C and N in individual clusters measured experimentally by APT and simulated using MC. Experimental measurements and MC simulations are performed for samples of Fe-3.28at.%Cr with varying low concentrations of defects. Analysis is performed with MSM. MC compositions are 0.007 % C, 0.028% N, 0/0.005/0.01% Vac.

be seen from this figure, the concentration of Cr from both MC simulations and experimental measurements is within the same boundaries. Taking into account the fact that the multiple-hit loss effect does not affect the detection of Cr in the experiments, and the deviation of Cr concentration due to the choice of MSM parameters being smaller than the range of concentrations detected, the correspondence between simulations and experiments is better than satisfactory.

It should be reminded that since vacancies are treated as another type of atom in MC simulations from the current work and there is no way for them to disappear from the simulated lattice, the equilibrium is reached when the exchanges of atoms (including Vac) do not lead to the significant changes of free energy, but instead make it fluctuate around "equilibrium" value. As such, this thermal equilibrium is different to real world thermal equilibrium, where thermal effects happen, such as Frenkel pair annihilation of evaporation of vacancies to various sinks. This is another motivation for running sets of MC simulations with a wide range of vacancy concentrations (see Fig. 11) Having the experimental results for Cr concentration in the clusters (30-60%), we can therefore set a limit to the Vac concentration according to MC simulations as not exceeding 0.02 at.%.

Current MC model does not allow for the investigation of line defects, however it allows for identifying the differences in the cluster structure depending on the local concentration of C, N, and vacancies (see Section 5).

8. Conclusions

In this work, we created a model for Fe-Cr system with vacancies and C/N interstitial impurities using a large set of DFT calculations of ordered and disordered phases of various with and without defects. Binding energy as well as stability of ordered phases both play roles in the resulting atomic structure observed in MC simulations: while Vac-Vac binding is clearly responsible for the formation of the voids, the binding of Vac-C is lower than Vac-N, and the more frequent segregation of C to the Voids is likely caused by more dominant segregation of N to Cr clusters, which is in turn caused by the high stability of ordered α-cementite-like $[Fe_xCr_y]_3[C_aN_b]$ phases with high N content.

In correspondence with the existing knowledge, the MC simulations at 650K based on our model show no precipitation of Cr below the solubility limit (3.28 at.% Cr) in the non-defected Fe-Cr alloy as well as in alloy with various concentration of vacancies, which is in line with the repulsive nature of Cr-Cr binding and significantly stronger binding of Vac-Vac compared to Vac-Cr.

With the addition of interstitials, starting at 0.01 at.%, the Cr-enriched clusters appear in MC simulations. The structure of such Cr-enriched precipitates, as well as defect clusters, depends on the local concentration of C, N and vacancies. In general, the increased concentration of vacancies suppresses the formation of Cr-enriched clusters by forming compact Vac-C-N clusters (gas bubbles or graphite precipitations) instead. The interstitial defects, on the other hand, increase the concentration of Cr inside the clusters, N showing higher potential for such an increase compared to C.

APT measurements of two samples provide a qualitatively similar picture of Cr segregating into clusters with increased concentration of C and N in them and their vicinity. Analysis of APT results also allowed for the identification of other microstructural features attracting Cr, namely dislocation lines and dislocation loops, however, in smaller amount

compared to clusters.

The qualitative agreement between the MC simulations and APT measurements for the concentration of Cr in the clusters gives credibility to the mechanisms of clustering.

9. Acknowledgements

This work has been carried out within the framework of the EUROfusion Consortium, funded by the European Union via the Euratom Research and Training Programme (Grant Agreement No 101052200 — EUROfusion). Views and opinions expressed are however those of the author(s) only and do not necessarily reflect those of the European Union or the European Commission. Neither the European Union nor the European Commission can be held responsible for them. The research used UKAEA's Materials Research Facility, which has been funded by and is a part of the UK National Nuclear User Facility and Henry Royce Institute for Advanced Materials. AJL, SLD and DNM acknowledge funding from the RCUK Energy Programme Grant No. EP/W006839/1. The work at WUT has been carried out as a part of an international project co-financed by the Polish Minister of Science and Higher Education through the PMW program in 2019; Agreement No. 5018 / H2020-Euratom / 2019/2. JSW and DNM would like to acknowledge the use of high-performance computing facility MARCONI (Bologna, Italy) provided by EUROfusion.

References

[1] D. Stork, P. Agostini, J.-L. Boutard, D. Buckthorpe, E. Diegele, S.L. Dudarev, C. English, G. Federici, M.R. Gilbert, S. Gonzalez, A. Ibarra, C. Linsmeier, A.L. Puma, G. Marbach, L.W. Packer, B. Raj, M. Rieth, M.Q. Tran, D.J. Ward, and S.J. Zinkle. Materials R&D for a timely DEMO: Key findings and recommendations of the EU Roadmap Materials Assessment Group. *Fusion Eng. Des.*, 89(7):1586–1594, 2014.

[2] R. Lindau, A. Möslang, and M. Schirra. Thermal and mechanical behaviour of the reduced-activation-ferritic-martensitic steel EUROFER. *Fusion Eng. Des.*, 61-62:659–664, 2002.

[3] E. Lucon, P. Benoit, P. Jacquet, E. Diegele, R. Lässer, A. Alamo, R. Coppola, F. Gillemot, P. Jung, A. Lind, S. Messoloras, P. Novosad, R. Lindau, D. Preininger, M. Klimiankou, C. Petersen, M. Rieth, E. Materna-Morris, H.-C. Schneider, J.-W. Rensman, B. van der Schaaf, B.K. Singh, and P. Spaetig. The European effort towards the development of a demo structural material: Irradiation behaviour of the European reference RAFM steel EUROFER. *Fusion Eng. Des.*, 81(8):917–923, 2006.

[4] C.D. Hardie, C.A. Williams, S. Xu, and S.G. Roberts. Effects of irradiation temperature and dose rate on the mechanical properties of self-ion implanted Fe and Fe–Cr alloys. *J. Nucl. Mater.*, 439(1-3):33–40, 2013.

[5] J.C. Haley, S. de Moraes Shubeita, P. Wady, A.J. London, G.R. Odette, S. Lozano-Perez, and S.G. Roberts. Microstructural examination of neutron, proton and self-ion irradiation damage in a model Fe9Cr alloy. *J. Nucl. Mater.*, 533:152130, 2020.

[6] S. Hari Babu, R. Rajaraman, G. Amarendra, R. Govindaraj, N.P. Lalla, A. Dasgupta, G. Bhalerao, and C.S. Sundar. Dislocation driven chromium precipitation in Fe-9Cr binary alloy: A positron lifetime study. *Philos. Mag.*, 92(23):2848–2859, 2012.

[7] V. Kuksenko, C. Pareige, and P. Pareige. Cr precipitation in neutron irradiated industrial purity Fe-Cr model alloys. *J. Nucl. Mater.*, 432(1-3):160–165, 2013.

[8] W. Xiong, M. Selleby, Q. Chen, J. Odqvist, and Y. Du. Phase equilibria and thermodynamic properties in the Fe-Cr system. *Critical Reviews in Solid State and Materials Sciences*, 35(2):125–152, 2010.

[9] Z. Jiao and G.S. Was. Segregation behavior in proton- and heavy-ion-irradiated ferritic-martensitic alloys. *Acta Mater.*, 59(11):4467–4481, 2011.

[10] P.M. Derlet and S.L. Dudarev. Microscopic structure of a heavily irradiated material. *Phys. Rev. Materials*, 4(2):023605, 2020.

[11] M.J. Swenson and J.P. Wharry. Nanocluster irradiation evolution in Fe-9%Cr ODS and ferritic-martensitic alloys. *J. Nucl. Mater.*, 496:24–40, 2017.

[12] M. Bachhav, G.R. Odette, and E.A. Marquis. Microstructural changes in a neutron-irradiated Fe-15 at.%Cr alloy. *J. Nucl. Mater.*, 454(1):381–386, 2014.

[13] M. Bachhav, G.R. Odette, and E.A. Marquis. α' precipitation in neutron-irradiated Fe-Cr alloys. *Scr. Mater.*, 74:48–51, 2014.

[14] C. Domain, C.S. Becquart, and J. Foct. Ab initio study of foreign interstitial atom (C, N) interactions with intrinsic point defects in α-Fe. *Phys. Rev. B*, 69(14):1–16, 2004.

[15] C.J. Först, J. Slycke, K.J. Van Vliet, and S. Yip. Point defect concentrations in metastable fe-c alloys. *Phys. Rev. Lett.*, 96:175501, 2006.

[16] T. Jourdan, C.-C. Fu, L. Joly, J.L. Bocquet, M.J. Caturla, and F. Willaime. Direct simulation of resistivity recovery experiments in carbon-doped α-iron. *Phys. Scr.*, T145:014049, 2011.

[17] C. Barouh, T. Schuler, C.-C. Fu, and M. Nastar. Interaction between vacancies and interstitial solutes (C, N, and O) in α-Fe: From electronic structure to thermodynamics. *Phys. Rev. B*, 90(5):054112, 2014.

[18] M.Yu Lavrentiev, D. Nguyen-Manh, and S.L. Dudarev. Chromium-vacancy clusters in dilute bcc Fe-Cr alloys: An ab initio study. *J. Nucl. Mater.*, 499:613–621, 2018.

[19] G. Bonny, A. Bakaev, and D. Terentyev. Energetic Stability of Vacancy-Carbon Clusters in Solid Solution Alloys: The Fe-Cr-C Case. *Phys. Status Solidi B*, 256(11):1–6, 2019.

[20] O. Senninger, F. Soisson, E. Martinez, M. Nastar, C.-C. Fu, and Y. Brechet. Modeling radiation induced segregation in iron-chromium alloys. *Acta Mater.*, 103:1–11, 2016.

[21] R. Herschberg, C.-C. Fu, M. Nastar, and F. Soisson. Atomistic modelling of the diffusion of C in Fe–Cr alloys. *Acta Mater.*, 165:638–653, 2019.

[22] M. Chiapetto, L. Malerba, A. Puype, and C.S. Becquart. Object kinetic Monte Carlo study of the effect of grain boundaries in martensitic Fe–Cr–C alloys. *Phys. Status Solidi A*, 213(11):2981–2987, 2016.

[23] J.S. Wróbel, D. Nguyen-Manh, K.J. Kurzydłowski, and S.L. Dudarev. A first-principles model for anomalous segregation in dilute ternary tungsten-rhenium-vacancy alloys. *J. Phys. Condens. Matter*, 29(14):145403, 2017.

[24] D. Nguyen-Manh, J.S. Wróbel, M. Klimenkov, M.J. Lloyd, L. Messina, and S.L. Dudarev. First-principles model for voids decorated by transmutation solutes: Short-range order effects and application to neutron irradiated tungsten. *Phys. Rev. Materials*, 5:065401, 2021.

[25] G. Kresse and J. Hafner. Ab initio molecular dynamics for liquid metals. *Phys. Rev. B*, 47(1):558–561, 1993.

[26] G. Kresse and J. Hafner. *Ab initio* molecular-dynamics simulation of the liquid-metal–amorphous-semiconductor transition in germanium. *Phys. Rev. B*, 49(20):14251–14269, 1994.

[27] G. Kresse and J. Furthmüller. Efficiency of ab-initio total energy calculations for metals and semiconductors using a plane-wave basis set. *Comput. Mater. Sci.*, 6(1):15–50, 1996.

[28] G. Kresse and J. Furthmüller. Efficient iterative schemes for ab initio total-energy calculations using a plane-wave basis set. *Phys. Rev. B*, 54(16):11169–11186, 1996.

[29] P.E. Blöchl. Projector augmented-wave method. *Phys. Rev. B*, 50(24):17953–17979, 1994.

[30] G. Kresse and D. Joubert. From ultrasoft pseudopotentials to the projector augmented-wave method. *Phys. Rev. B*, 59(3):1758–1775,

1999.

[31] J.P. Perdew, K. Burke, and M. Ernzerhof. Generalized gradient approximation made simple. *Phys. Rev. Lett.*, 77(18):3865–3868, 1996.

[32] J.D. Pack and H.J. Monkhorst. Special points for Brillouin-zone integrations. *Phys. Rev. B*, 13(12):5188–5192, 1976.

[33] A. van de Walle and G. Ceder. Automating first-principles phase diagram calculations. *J. Phase Equilib.*, 23(4):348–359, 2002.

[34] A. van de Walle and M. Asta. Self-driven lattice-model Monte Carlo simulations of alloy thermodynamic properties and phase diagrams. *Model. Simul. Mater. Sci. Eng. A*, 10(5):521–538, 2002.

[35] A. van de Walle. Multicomponent multisublattice alloys, nonconfigurational entropy and other additions to the Alloy Theoretic Automated Toolkit. *CALPHAD*, 33(2):266–278, 2009.

[36] G.L.W. Hart and R.W. Forcade. Algorithm for generating derivative structures. *Phys. Rev. B*, 77(22):224115, 2008.

[37] O. Buggenhoudt. *Modelling and simulation of carbides in alpha-Fe alloys from first principles : alloying elements, diffusion and nucleation*. PhD thesis, Université Paris-Saclay, 2021.

[38] See supplemental material at [url will be inserted by publisher] for additional information not fit for the main part of the manuscript, including the intermediate data from cluster expansion and a more detailed analysis of defect clusters.

[39] J. Le Coze. Procurement of pure Fe metal and Fe-based alloys with controlled chemical alloying element contents and microstructure. *ARMINES Ecole Nationale Superieure des Mines*, 2007.

[40] C.D. Hardie, A.J. London, J.J.H. Lim, R. Bamber, T. Tadić, M. Vukšić, and S. Fazinić. Exploitation of thermal gradients for investigation of irradiation temperature effects with charged particles. *Sci. Rep.*, 9:13541, 2019.

[41] W.C. Oliver and G.M. Pharr. An improved technique for determining hardness and elastic modulus using load and displacement sensing indentation experiments. *J. Mater. Res.*, 7:1564–1583, 1992.

[42] M.K. Miller, K.F. Russell, K. Thompson, R. Alvis, and D.J. Larson. Review of atom probe FIB-based specimen preparation methods. *Microsc. Microanal.*, 13(6):428–436, 2007.

[43] J.M. Hyde and C.A. English. Microstructural processes in irradiated materials. In *MRS 2000 Fall Meet. Symp. Boston, MA*, pages 27–29, 2001.

[44] L.T. Stephenson, M.P. Moody, P.V. Liddicoat, S.P. Ringer, S. Byers, A.E. Rafferty, A. Cerezo, L. Davin, P.J. Clark, F.C. Evans, and Others. New techniques for the analysis of fine-scaled clustering phenomena within atom probe tomography (APT) data. *Microsc. Microanal.*, 13(6):448–463, 2007.

[45] C.A. Williams, D. Haley, E.A. Marquis, G.D.W. Smith, and M.P. Moody. Defining clusters in APT reconstructions of ODS steels. *Ultramicroscopy*, 132:271–278, 2013.

[46] M.Yu Lavrentiev, R. Drautz, D. Nguyen-Manh, T.P.C. Klaver, and S.L. Dudarev. Monte Carlo study of thermodynamic properties and clustering in the bcc Fe-Cr system. *Phys. Rev. B*, 75(1):1–12, 2007.

[47] J.S. Wróbel, D. Nguyen-Manh, M.Yu. Lavrentiev, M. Muzyk, and S.L. Dudarev. Phase stability of ternary fcc and bcc Fe-Cr-Ni alloys. *Phys. Rev. B*, 91:024108, 2015.

[48] C. Domain and C.S. Becquart. Ab initio calculations of defects in Fe and dilute Fe-Cu alloys. *Phys. Rev. B*, 65(December):024103, 2001.

[49] A. Bakaev, D. Terentyev, X. He, E.E. Zhurkin, and D. Van Neck. Interaction of carbon-vacancy complex with minor alloying elements of ferritic steels. *J. Nucl. Mater.*, 451(1-3):82–87, 2014.

[50] G. Bonny, R.C. Pasianot, L. Malerba, A. Caro, P. Olsson, and M.Yu Lavrentiev. Numerical prediction of thermodynamic properties of iron-chromium alloys using semi-empirical cohesive models: The state of the art. *J. Nucl. Mater.*, 385(2):268–277, 2009.

[51] D.R. Mason, F. Granberg, M. Boleininger, T. Schwarz-Selinger, K. Nordlund, and S.L. Dudarev. Parameter-free quantitative simulation of high-dose microstructure and hydrogen retention in ion-irradiated tungsten. *Phys. Rev. Materials*, 5:095403, 2021.

[52] G.S. Was, S. Taller, Z. Jiao, A.M. Monterrosa, D. Woodley, D. Jennings, T. Kubley, F. Naab, O. Toader, and E. Uberseder. Resolution of the carbon contamination problem in ion irradiation experiments. *Nucl. Instrum. Methods Phys. Res. B*, 412:58–65, 2017.

[53] A.J. London, S. Lozano-Perez, M.P. Moody, S. Amirthapandian, B.K. Panigrahi, C.S. Sundar, and C.R.M. Grovenor. Quantification of oxide particle composition in model oxide dispersion strengthened steel alloys. *Ultramicroscopy*, 159:360–367, 2015.

[54] B. Gault, F. Danoix, K. Hoummada, D. Mangelinck, and H. Leitner. Impact of directional walk on atom probe microanalysis. *Ultramicroscopy*, 113:182–191, 2012.

[55] M. Thuvander, A. Kvist, L.J.S. Johnson, J. Weidow, and H.-O. Andrén. Reduction of multiple hits in atom probe tomography. *Ultramicroscopy*, 132:81–85, 2013.

[56] E.A. Jägle, P.-P. Choi, and D. Raabe. The maximum separation cluster analysis algorithm for atom-probe tomography: Parameter determination and accuracy. *Microsc. Microanal.*, 20(6):1662–1671, 2014.